

# Electroelastodynamics of flexoelectric energy conversion and harvesting in elastic dielectrics

Adriane G. Moura and Alper Erturk<sup>a)</sup>

G. W. Woodruff School of Mechanical Engineering, Georgia Institute of Technology, Atlanta, Georgia 30332, USA

(Received 15 December 2016; accepted 29 January 2017; published online 14 February 2017)

Flexoelectricity is the generation of electric polarization by the application of a non-uniform mechanical strain field, i.e., a strain gradient. This phenomenon is exhibited by all elastic dielectrics, but is expected to be significant only at very small scales. Energy harvesting is a potential future application area of flexoelectricity to enable next-generation ultra-low-power MEMS/NEMS devices by converting ambient vibrations into electricity. In this paper, an electroelastodynamic framework is presented and analyzed for flexoelectric energy harvesting from strain gradient fluctuations in centrosymmetric dielectrics, by accounting for the presence of a finite electrical load across the surface electrodes as well as two-way electromechanical coupling, and capturing the size effect. The flexoelectric energy harvester model is based on the Euler-Bernoulli beam theory and it assumes the main source of polarization to be static bulk flexoelectricity. Following recent efforts on the converse flexoelectric effect in finite samples, the proposed model properly accounts for thermodynamically consistent, symmetric direct and converse coupling terms. The transverse mode flexoelectric coupling coefficient ( $k$ ) is obtained analytically as a direct measure of energy conversion; its dependence on the cantilever thickness and a material Figure of Merit (FoM) is shown. Size effects are further demonstrated by simulations of the electromechanical frequency response for a Strontium Titanate (STO) energy harvester at different geometric scales. It is obtained that the flexoelectric coupling coefficient of an STO cantilever for the fundamental bending mode increases from  $k \approx 3.5 \times 10^{-7}$  to  $k \approx 0.33$  as the thickness is reduced from mm- to nm-level. A critique of the experimentally identified large flexoelectric coefficient for Barium Strontium Titanate (BST) from the literature is also given with a coupling coefficient perspective. *Published by AIP Publishing.* [<http://dx.doi.org/10.1063/1.4976069>]

## I. INTRODUCTION

Microelectromechanical systems (MEMS) and nanoelectromechanical systems (NEMS) have received growing attention in the last decade for various applications including mechanical energy harvesting at very small scales.<sup>1-4</sup> The mechanical energy in this context spans from structure-borne vibrations<sup>5</sup> and waves<sup>6,7</sup> to rigid-body motions,<sup>8,9</sup> acoustic energy,<sup>10-12</sup> as well as aeroelastic<sup>13,14</sup> and hydroelastic<sup>15,16</sup> vibrations. In harvesting various forms of mechanical energy, piezoelectricity remains arguably the most widely studied transduction method with examples ranging from PZT-based (lead zirconate titanate) ferroelectric thin-films<sup>3</sup> to piezoelectric nanowires<sup>4</sup> employing non-ferroelectrics, such as ZnO (zinc oxide). It is well known that the *electromechanical coupling*<sup>17</sup> of piezoelectric materials diminishes dramatically in thin films<sup>18</sup> and polymers.<sup>19</sup> Piezoelectric polymers, such as PVDF (polyvinylidene fluoride), are environmentally benign as compared to ceramics but they are poor power generators due to low electromechanical coupling. Bulk piezoelectric ceramics (such as PZT-5A and PZT-5H) are relatively brittle and less reliable for powering sensor systems in harsh environments. Moreover, lead content in most piezoelectric ceramic compositions is a major

environmental issue.<sup>20</sup> Furthermore, several of the high electromechanical coupling materials lose their piezoelectricity at moderate to high temperatures, where self-powered sensors are most needed.

Recent efforts at small scales<sup>21</sup> suggest that the *effective* electromechanical properties of elastic dielectrics can be enhanced dramatically under non-uniform strain fields due to an entirely different phenomenon called *flexoelectricity*.<sup>22-27</sup> Flexoelectricity describes the generation of electric polarization in elastic dielectrics by the application of a mechanical strain gradient.<sup>23,25,28</sup> The phenomenon of flexoelectricity in solids is a higher-order effect and is expected to be rather weak except for very small (sub-micron) dimensions, making the concept of interest mainly for potential MEMS and especially NEMS applications.

Following the early efforts by Mashkevich and Tolpygo,<sup>29</sup> Kogan,<sup>30</sup> and Indenbom *et al.*,<sup>31</sup> the first comprehensive theoretical discussion of the flexoelectric effect was presented by Tagantsev.<sup>22</sup> The research field of flexoelectricity has been active for liquid crystals<sup>32</sup> and biological matter<sup>33</sup> for decades. However, it was only in early 2000s the flexoelectric effect in solids has received suddenly growing attention especially after the experiments by Ma and Cross<sup>34-39</sup> on elastic dielectrics, specifically high- $K$  materials such as ferroelectric perovskites (see the review article by Cross<sup>40</sup>). In addition to experimental efforts by Ma and

<sup>a)</sup>Author to whom correspondence should be addressed. Electronic mail: alper.erturk@me.gatech.edu

Cross<sup>34–39</sup> and others<sup>41–43</sup> for samples with high dielectric constants, atomistic simulations<sup>28</sup> were presented to extract flexoelectric coefficients. Importantly, a substantial difference (several orders of magnitude) was reported between the simulated and identified flexoelectric coefficients.<sup>39</sup> The experimental samples<sup>34–39</sup> (of  $\sim$ mm thickness) used in the identification efforts were typically far from the thickness levels of interest ( $\sim$ nm) in flexoelectricity. A comprehensive article on the flexoelectric effect in solids by Yudin and Tagantsev<sup>25</sup> presents a detailed discussion on the subject matter along with a historical account. It is no surprise that, with its promise of increased electromechanical coupling at small scales, flexoelectricity is of great interest for sub-micron level energy harvesting<sup>44,45</sup> to power next-generation nanoscale sensors and other extremely low-power small electronic components.

Other than the mismatch in the order of magnitude of flexoelectric coupling between atomistic simulations<sup>28</sup> and experimental measurements,<sup>34–39</sup> one of the issues in flexoelectric transduction and energy conversion has been the lack of a clear understanding and modeling of the converse effect, as the subject has created confusion since the converse effect is represented by a polarization gradient.<sup>46–48</sup> In a recent work focusing on finite samples, Tagantsev and Yurkov<sup>49</sup> presented a consistent and symmetric converse effect representation and its justification. In the present work, we combine the direct effect of flexoelectricity and this symmetric converse effect<sup>49</sup> within a distributed-parameter electroelastodynamic framework and provide a modal analysis solution for vibration energy harvesting from base excitation of dielectric cantilevers. In addition to closed-form expressions for the electromechanically coupled voltage across the electrical load and the shunted vibration response (that accounts for the effect of the electrical load), the size-dependent flexoelectric coupling coefficient is extracted analytically, and a figure of merit is identified. Simulation case studies are given for transverse vibrations of a cantilevered Strontium Titanate (STO) energy harvester at different geometric scales to explore the effect of thickness on flexoelectric energy conversion as well as the effect of power generation on the harvester structure due to converse coupling.

## II. DIRECT AND CONVERSE FLEXOELECTRIC EFFECTS

We consider the problem of a centrosymmetric thin cantilever under mechanical base excitation (Fig. 1) for linear

transverse (bending) vibrations, i.e., linear electroelastic material behavior and geometrically small oscillations are assumed in this continuum framework. The surface electrodes of the cantilever are shunted to a resistive electrical load to quantify the electrical power output in the harvester model. The sample geometry justifies thin beam assumptions, such that the width ( $b$ ) and the thickness ( $h$ ) of the rectangular cross section are much smaller than the overhang length ( $L$ ). “Static” flexoelectricity<sup>25</sup> is applicable since the thickness (smallest dimension) of the beam is much smaller than the wavelength at vibration frequencies of interest in this work for the first few bending modes. In the following, the focus is placed on static bulk flexoelectricity, and therefore, the surface effects<sup>24,25</sup> are excluded.

The polarization including the *direct* flexoelectric effect can be written as

$$P_3 = \chi_{33}E_3 + \mu_{1133} \frac{\partial S_{11}}{\partial x_3}, \quad (1)$$

where  $P_3$  is the polarization in the thickness direction (3-direction is the thickness direction and 1-direction is the axial direction in Fig. 1),  $E_3$  is the electric field,  $S_{11}$  is the axial strain,  $\chi_{33}$  is the dielectric susceptibility (which has the units of F/m, and should not be confused with the dimensionless electric susceptibility form  $\bar{\chi}_{33}$ ,  $\chi_{33} = \bar{\chi}_{33}\epsilon_0$ , where  $\epsilon_0$  is the vacuum permittivity), and  $\mu_{1133}$  is the transverse flexoelectric coefficient. Note that the fourth-rank static flexoelectric coefficient tensor is defined as<sup>24,25</sup>  $\mu_{kl ij} = (\partial P_i / \partial (\partial S_{kl} / \partial x_j))_{E=0}$  and we stick to this complete index notation, while some authors<sup>39</sup> use the contracted notation  $\mu_{12}$  for the transverse mode flexoelectric coefficient  $\mu_{1133}$  (for detailed discussions of flexoelectric tensors and symmetry arguments, see recent papers by Quang and He,<sup>50</sup> and Shu *et al.*<sup>51</sup>).

The mechanical stress accounting for the *converse* flexoelectric effect can be expressed as

$$T_{11} = c_{1111}S_{11} + f_{1133} \frac{\partial P_3}{\partial x_3} \quad (2)$$

or alternatively

$$T_{11} = c_{1111}S_{11} + \mu_{1133} \frac{\partial E_3}{\partial x_3}, \quad (3)$$

where  $T_{11}$  is the axial stress,  $c_{1111}$  is the elastic modulus (under short-circuit condition of the electrodes), and  $f_{1133}$  is the transverse mode “flexocoupling coefficient”<sup>25</sup> ( $f_{1133} = \chi_{33}^{-1}\mu_{1133}$ ).

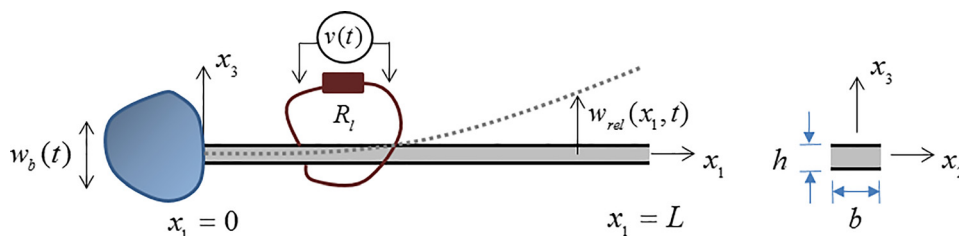


FIG. 1. Base-excited centrosymmetric dielectric cantilever with surface electrodes (that are perpendicular to the thickness direction) connected to a resistive electrical load for energy harvesting, and a cross-sectional view. The transverse displacement of the beam relative to the moving base is  $w_{rel}$  and the voltage output across the resistive load is  $v$ .

Note that the approximate flexocoupling coefficient order of magnitude<sup>24</sup> is 1–10 V based on Kogan's estimate<sup>30</sup>  $f \approx q/(4\pi\epsilon_0 a)$ , where  $q$  and  $a$  are the lattice charge and spacing, respectively (this order of magnitude is in agreement with recently presented upper bounds by Yudin *et al.*<sup>52</sup>).

### III. FLEXOELECTRIC EULER-BERNOULLI BEAM MODEL FOR ENERGY HARVESTING

#### A. Flexoelectrically coupled mechanical equation and modal analysis

The partial differential equation governing the forced vibration of a uniform cantilevered centrosymmetric thin dielectric beam under transverse base excitation (Fig. 1) is

$$-\frac{\partial^2 M(x_1, t)}{\partial x_1^2} + c_s I \frac{\partial^5 w_{rel}(x_1, t)}{\partial x_1^4 \partial t} + c_a \frac{\partial w_{rel}(x_1, t)}{\partial t} + m \frac{\partial^2 w_{rel}(x_1, t)}{\partial t^2} = -m \frac{d^2 w_b(t)}{dt^2}, \quad (4)$$

where  $w_b(t)$  is the base excitation (in the form of displacement),  $w_{rel}(x_1, t)$  is the transverse displacement of the beam (reference surface, or neutral axial level) relative to its base and  $M(x_1, t)$  is the internal bending moment at position  $x_1$  and time  $t$ ,  $c_a$  is the viscous air damping coefficient (as a mass-proportional dissipative term),  $c_s$  is the strain-rate damping coefficient (as a stiffness-proportional dissipative term), and  $m$  is the mass per unit length of the beam ( $m = \rho b h$  where  $\rho$  is the mass density of the beam material). In the same vein as cantilevered piezoelectric energy harvester counterparts,<sup>53,54</sup> the linear damping operators in Eq. (4) satisfy the proportional damping condition so that the mode shapes of the corresponding undamped system can be used in modal analysis (implementation of nonlinear intrinsic and extrinsic damping mechanisms is beyond the scope of this work – see Leadenham and Erturk,<sup>55,56</sup> among others, for the resonant modeling of quadratic solid<sup>55</sup> and fluid<sup>56</sup> damping).

The internal bending moment in Eq. (4) is the first moment of the axial stress field over the cross-section

$$M(x_1, t) = b \int_{-h/2}^{h/2} T_{11} x_3 dx_3. \quad (5)$$

The axial strain component is due to bending only and it can be expressed as

$$S_{11}(x_1, x_3, t) = -x_3 \frac{\partial^2 w_{rel}(x_1, t)}{\partial x_1^2}. \quad (6)$$

It is clear from Eqs. (1) and (6) that the *strain gradient*  $\partial S_{11}/\partial x_3$  in this model is nothing but the negative *curvature* of the uniform Euler-Bernoulli beam (assuming the effect of the gradient  $\partial S_{11}/\partial x_1$  to be negligible).

Substituting Eqs. (2) and (6) into the internal bending moment in Eq. (5) gives

$$M(x_1, t) = b \left( \int_{-h/2}^{h/2} c_{1111} S_{11} x_3 dx_3 + \int_{-h/2}^{h/2} f_{1133} \frac{\partial P_3}{\partial x_3} x_3 dx_3 \right). \quad (7)$$

Following Tagantsev and Yurkov,<sup>49</sup> for a finite sample in which the polarization in the thickness direction varies continuously from its bulk value to zero at the top and bottom surfaces of the cantilever at  $x_3 = h/2$  and  $x_3 = -h/2$  (based on the blocking boundary condition assumption—see Fig. 12(a) in Yudin and Tagantsev<sup>25</sup>), the second right-hand-side term can be evaluated using integration by parts to identify the role of this term in the moment equation

$$b f_{1133} \int_{-h/2}^{h/2} \frac{\partial P_3}{\partial x_3} x_3 dx_3 = -b f_{1133} \int_{-h/2}^{h/2} P_3 dx_3 = -b f_{1133} h \langle P_3 \rangle, \quad (8)$$

where  $\langle P_3 \rangle$  is the average polarization induced by the electric field in the beam. The spatial scale of the polarization variation at the dielectric-electrode interface is much smaller than that in the overall thickness  $h$ ; therefore, this average polarization is approximately the polarization in the bulk<sup>25,49</sup>

$$\langle P_3 \rangle \approx \chi_{33} E_3, \quad (9)$$

and it is useful to recall from Eqs. (2) and (3) that the dielectric susceptibility  $\chi_{33}$  is

$$\chi_{33} = \frac{\mu_{1133}}{f_{1133}}. \quad (10)$$

The electric field  $E_3$  can be given in terms of the voltage ( $v$ ) across the surface electrodes and the electrode spacing as  $E_3 = -v/h$  (where it is assumed that the electrode thickness is negligible). The flexoelectric term in Eq. (8) is only a function of time, and therefore, we multiply it by  $[H(x_1) - H(x_1 - L)]$  (where  $H(x_1)$  is the Heaviside function), to ensure the survival of this term when the bending moment is substituted into Eq. (4), for full electrode coverage (Fig. 1) from the clamped end ( $x_1 = 0$ ) to the free end ( $x_1 = L$ ). The internal bending moment is then

$$M(x_1, t) = -YI \frac{\partial^2 w_{rel}(x_1, t)}{\partial x_1^2} + \mu_{1133} b v(t) [H(x_1) - H(x_1 - L)], \quad (11)$$

where the flexural rigidity  $YI$  for the rectangular cross section (under short-circuit condition) is

$$YI = \frac{c_{1111} b h^3}{12}. \quad (12)$$

The flexoelectrically coupled centrosymmetric Euler-Bernoulli beam equation for transverse vibrations can then be obtained from Eq. (4) as

$$\begin{aligned}
& YI \frac{\partial^4 w_{rel}(x_1, t)}{\partial x_1^4} + c_s I \frac{\partial^5 w_{rel}(x_1, t)}{\partial x_1^4 \partial t} + c_a \frac{\partial w_{rel}(x_1, t)}{\partial t} \\
& + m \frac{\partial^2 w_{rel}(x_1, t)}{\partial t^2} - \mu_{1133} b v(t) \left[ \frac{d\delta(x_1)}{dx_1} - \frac{d\delta(x_1 - L)}{dx_1} \right] \\
& = -m \frac{d^2 w_b(t)}{dt^2}, \tag{13}
\end{aligned}$$

where  $\delta(x_1)$  is the Dirac delta function that satisfies the following equation for a smooth test function  $\gamma(x_1)$ :

$$\int_{-\infty}^{\infty} \frac{d^{(n)}\delta(x_1 - p)}{dx_1^{(n)}} \gamma(x_1) dx_1 = (-1)^n \frac{d\gamma^{(n)}(p)}{dx_1^{(n)}}. \tag{14}$$

The vibration response (transverse displacement of the reference surface) relative to the moving base in Fig. 1 can be expressed as

$$w_{rel}(x_1, t) = \sum_{r=1}^{\infty} \phi_r(x_1) \eta_r(t). \tag{15}$$

Here,  $\eta_r(t)$  is the modal mechanical coordinate and  $\phi_r(x_1)$  is the mass-normalized eigenfunction (obtained from the short-circuit problem) for the  $r$ -th vibration mode

$$\begin{aligned}
\phi_r(x_1) = & \sqrt{\frac{1}{mL}} \left[ \cos \frac{\lambda_r x_1}{L} - \cosh \frac{\lambda_r x_1}{L} \right. \\
& \left. + \sigma_r \left( \sin \frac{\lambda_r x_1}{L} - \sinh \frac{\lambda_r x_1}{L} \right) \right], \tag{16}
\end{aligned}$$

where

$$\sigma_r = \frac{\sin \lambda_r - \sinh \lambda_r}{\cos \lambda_r + \cosh \lambda_r}, \tag{17}$$

and the eigenvalues ( $\lambda_r > 0, r = 1, 2, \dots$ ) are the roots of the characteristic equation (for the short-circuit and clamped-free boundary conditions)

$$1 + \cos \lambda \cosh \lambda = 0. \tag{18}$$

The mass-normalized eigenfunctions in Eq. (15) satisfy the following orthogonality conditions:

$$\int_0^L m \phi_r(x_1) \phi_s(x_1) dx_1 = \delta_{rs}, \quad \int_0^L YI \phi_r(x_1) \frac{d^4 \phi_s(x_1)}{dx_1^4} dx_1 = \delta_{rs} \omega_r^2, \tag{19}$$

where  $\delta_{rs}$  is the Kronecker delta and  $\omega_r$  is the undamped natural frequency of the  $r$ -th vibration mode under short-circuit conditions ( $R_l \rightarrow 0$ )

$$\omega_r = \lambda_r^2 \sqrt{\frac{YI}{mL^4}}, \tag{20}$$

which can also be denoted by  $\omega_r^{sc}$ , the short-circuit natural frequency of the  $r$ -th mode.

The mechanical equation in modal coordinates can be obtained after substituting Eq. (15) into Eq. (13) (then

multiplying the latter by the mode shape, integrating over the beam length, and applying the orthogonality conditions) as

$$\frac{d^2 \eta_r(t)}{dt^2} + 2\zeta_r \omega_r \frac{d\eta_r(t)}{dt} + \omega_r^2 \eta_r(t) - \theta_r v(t) = f_r(t), \tag{21}$$

where the modal electromechanical coupling term due to flexoelectricity is

$$\theta_r = \mu_{1133} b \left. \frac{d\phi_r(x_1)}{dx_1} \right|_{x_1=L}, \tag{22}$$

and modal mechanical forcing function can be expressed as

$$f_r(t) = -m \frac{d^2 w_b(t)}{dt^2} \int_0^L \phi_r(x_1) dx_1. \tag{23}$$

## B. Flexoelectrically coupled electrical circuit equation

In order to obtain an electrical circuit equation in the presence of a finite electrical load impedance, it is useful to express the electric displacement that is compatible with the polarization form of Eq. (1) through the well-known dielectric relationship

$$D_3 = P_3 + \epsilon_0 E_3. \tag{24}$$

Substituting Eq. (1) into Eq. (24), the non-zero electric displacement component for transverse vibrations of the thin beam configuration with surface electrodes shown in Fig. 1 becomes

$$D_3 = \epsilon_{33} E_3 + \mu_{1133} \frac{\partial S_1}{\partial x_3}, \tag{25}$$

where  $\epsilon_{33}$  is the dielectric permittivity  $\epsilon_{33} = \epsilon_0 + \chi_{33} = (1 + \bar{\chi}_{33})\epsilon_0$  (note that for high- $K$  materials, which are of interest in flexoelectricity,  $\bar{\chi}_{33} \gg 1$ , and  $\epsilon_{33} \approx \chi_{33}$ ).

In the presence of a finite resistive load connected across the electrodes of the beam, the flexoelectrically coupled circuit equation can be obtained from the integral

$$\frac{d}{dt} \left( \int_A \mathbf{D} \cdot \mathbf{n} dA \right) = \frac{v(t)}{R_l}, \tag{26}$$

where  $\mathbf{D}$  is the vector of electric displacement components,  $\mathbf{n}$  is the unit outward normal of the electrodes, and the integration is performed over the electrode area  $A$ . The only contribution to the inner product of the integrand is from  $D_3$  given by Eq. (25).

Using Eq. (25) in Eq. (26), the following circuit equation (current balance) is obtained:

$$C \frac{dv(t)}{dt} + \frac{v(t)}{R_l} + \mu_{1133} b \int_0^L \frac{\partial^3 w_{rel}(x_1, t)}{\partial x_1^2 \partial t} dx_1 = 0, \tag{27}$$

where the capacitance ( $C$ ) is

$$C = \frac{\varepsilon_{33}bL}{h}. \quad (28)$$

Note that, it is possible to introduce dielectric losses by changing the real-valued capacitance to  $C(1 - j \tan \delta)$  where  $\tan \delta$  is the loss tangent.

Equation (15) can be substituted into Eq. (28) to obtain

$$C \frac{dv(t)}{dt} + \frac{v(t)}{R_l} + \sum_{r=1}^{\infty} \theta_r \frac{d\eta_r(t)}{dt} = 0. \quad (29)$$

Here, the modal electromechanical coupling ( $\theta_r$ ) due to the *direct* flexoelectric effect is the same as Eq. (22) that was obtained for the *converse* effect, which further confirms the symmetry in the fully coupled governing electroelastodynamic equations, which are Eqs. (13) and (27) in physical coordinates, or Eqs. (21) and (29) in modal coordinates. Flexoelectric power generation as a result of voltage output across the resistive load is due to Eq. (27), and simultaneously the voltage output sends a feedback to the mechanical domain due to the voltage term in Eq. (13), as a manifestation of the thermodynamic consistency resulting from the two-way coupling.

### C. Closed-form voltage response and vibration response at steady state

For harmonic base excitation with  $w_b(t) = W_0 e^{j\omega t}$ , the modal forcing function given by Eq. (23) can be expressed as  $f_r(t) = F_r e^{j\omega t}$ , where the amplitude  $F_r$  is

$$F_r = \omega^2 m W_0 \int_0^L \phi_r(x_1) dx_1. \quad (30)$$

Then, the steady-state modal mechanical coordinate of the beam and the steady-state voltage response across the resistive load are also harmonic at the same frequency as  $\eta_r(t) = H_r e^{j\omega t}$  and  $v(t) = V e^{j\omega t}$ , respectively, where the amplitudes  $H_r$  and  $V$  are complexed valued. Therefore, Eqs. (21) and (29) yield

$$(\omega_r^2 - \omega_r + j2\zeta_r \omega_r \omega) H_r - \theta_r V = F_r, \quad (31)$$

$$\left( \frac{1}{R_l} + j\omega C \right) V + j\omega \sum_{r=1}^{\infty} \theta_r H_r = 0, \quad (32)$$

where  $\zeta_r$  is the modal mechanical damping ratio (due to purely mechanical dissipation) that can easily be related to  $c_s$  and  $c_a$  as  $2\zeta_r \omega_r = c_s I \omega_r^2 / YI + c_a / m$ .

The steady-state voltage response is obtained from Eqs. (31) and (32) as

$$v(t) = \frac{\sum_{r=1}^{\infty} \frac{-j\omega \theta_r F_r}{\omega_r^2 - \omega^2 + j2\zeta_r \omega_r \omega}}{\frac{1}{R_l} + j\omega C + \sum_{r=1}^{\infty} \frac{j\omega \theta_r^2}{\omega_r^2 - \omega^2 + j2\zeta_r \omega_r \omega}} e^{j\omega t}. \quad (33)$$

Once the voltage across the electrical load is obtained, the current and power output can be calculated easily. For the

case of a real-valued electrical load (i.e., resistive load), the current delivered to the load is  $i(t) = v(t)/R_l$  and the instantaneous power output is  $P(t) = v^2(t)/R_l$ .

The steady-state modal mechanical response of the beam (that accounts for the converse effect) can be obtained as

$$w_{rel}(x_1, t) = \sum_{r=1}^{\infty} \left[ \left( F_r - \theta_r \frac{\sum_{r=1}^{\infty} \frac{j\omega \theta_r F_r}{\omega_r^2 - \omega^2 + j2\zeta_r \omega_r \omega}}{\frac{1}{R_l} + j\omega C + \sum_{r=1}^{\infty} \frac{j\omega \theta_r^2}{\omega_r^2 - \omega^2 + j2\zeta_r \omega_r \omega}} \right) \times \frac{\phi_r(x_1) e^{j\omega t}}{\omega_r^2 - \omega^2 + j2\zeta_r \omega_r \omega} \right]. \quad (34)$$

### IV. SIZE EFFECTS ON MODAL ELECTROMECHANICAL COUPLING COEFFICIENT

One direct measure of energy conversion is the electro-mechanical coupling coefficient “ $k$ ” as commonly used in piezoelectricity.<sup>17,57</sup> It is possible to analytically extract the transverse mode electromechanical coupling coefficient due to bulk flexoelectricity for the centrosymmetric cantilever of Fig. 1. A dynamic definition of the modal electromechanical coupling coefficient can be obtained based on the difference between the open-circuit and short-circuit natural frequencies<sup>17,57</sup>

$$k^2 = \frac{(\omega_r^{oc})^2 - (\omega_r^{sc})^2}{(\omega_r^{oc})^2}, \quad (35)$$

where  $k$  is the *flexoelectric coupling coefficient* for the  $r$ -th vibration mode (the focus in the simulations of this work will be placed on the fundamental mode,  $r = 1$ ). Square of the coupling coefficient, as well known from piezoelectric energy conversion problems, is a measure of how much of the mechanical work is converted to electrical energy, or vice versa in electrical actuation problems. A similar argument and an analogous expression can be given in terms of the open- and short-circuit stiffness terms under quasistatic conditions.<sup>17,57</sup>

In order to express the coupling coefficient using Eq. (35), recall that the undamped short-circuit natural frequency of the  $r$ -th vibration mode is

$$\omega_r^{sc} = \omega_r = \lambda_r^2 \sqrt{\frac{YI}{mL^4}}. \quad (36)$$

Then, for modal vibrations (dominated by the  $r$ -th mode) and under open-circuit conditions, Eq. (29) can be reduced to

$$v(t) = \frac{-\theta_r \eta_r(t)}{C}, \quad R_l \rightarrow \infty. \quad (37)$$

Substituting Eq. (37) into the modal mechanical equation, Eq. (21), the undamped open-circuit natural frequency of the  $r$ -th vibration mode becomes

$$(\omega_r^{oc})^2 = (\omega_r^{sc})^2 \left( 1 + \frac{\theta_r^2}{\omega_r^2 C} \right) \quad (38)$$

yielding

$$k^2 = \frac{\left( \frac{\theta_r^2}{\omega_r^2 C} \right)}{\left( 1 + \frac{\theta_r^2}{\omega_r^2 C} \right)} = \frac{\theta_r^2}{\omega_r^2 C + \theta_r^2}. \quad (39)$$

Here, the capacitance is given by Eq. (27) and the modal coupling term can be expressed as

$$\theta_r = \mu_{1133} b \frac{d\phi_r(x_1)}{dx_1} \Big|_{x_1=L} = \mu_{1133} b \frac{1}{\sqrt{mL}} \frac{\lambda_r}{L} \alpha_r, \quad (40)$$

where

$$\alpha_r = -\sin \lambda_r - \sinh \lambda_r + \frac{\sin \lambda_r - \sinh \lambda_r}{\cos \lambda_r + \cosh \lambda_r} (\cos \lambda_r - \cosh \lambda_r). \quad (41)$$

Equation (39) then becomes

$$k^2 = \frac{1}{\frac{c_{1111} \epsilon_{33}}{\mu_{1133}^2} \frac{\lambda_r^2}{12 \alpha_r^2} h^2 + 1}, \quad (42)$$

which clearly captures the thickness dependence of the modal flexoelectric coupling coefficient. Note that the fundamental (first) bending vibration mode ( $r = 1$ ) is typically of interest for energy harvesting using a linear cantilever under base excitation,<sup>53,54</sup> yielding  $\lambda_1 = 1.87510407$  and  $\alpha_1 = -1.46819102$  for the simulations in this work (the first mode shape is shown in Fig. 2(a)). It is worth mentioning that energy harvesting at higher vibration modes requires using segmented electrodes to avoid charge cancellation.<sup>53,54</sup> The fundamental bending mode results in no cancellation for continuous electrode coverage since the curvature is in phase throughout the length of the beam (Fig. 2(c)), i.e., there are no inflection points. Note that, 85% of the electric charge is produced by the first half of the cantilever, i.e.,  $0 \leq x_1 \leq L/2$ , according to Fig. 2(b) (since the integral of curvature is related to the electric charge according to current balance Eq. (27) and the curvature is maximum near the clamped end in Fig. 2(c)). From the electromechanical coupling standpoint, 85% of the modal electromechanical coupling  $\theta_1$  (which determines the coupling coefficient  $k$ ) is due to the region  $0 \leq x_1 \leq L/2$ , in view of Eq. (22) and Fig. 2(b).

In terms of the size effect, Eq. (42) shows that with decreased thickness ( $h$ ) the coupling coefficient ( $k$ ) increases. This equation also shows the effect of the material properties

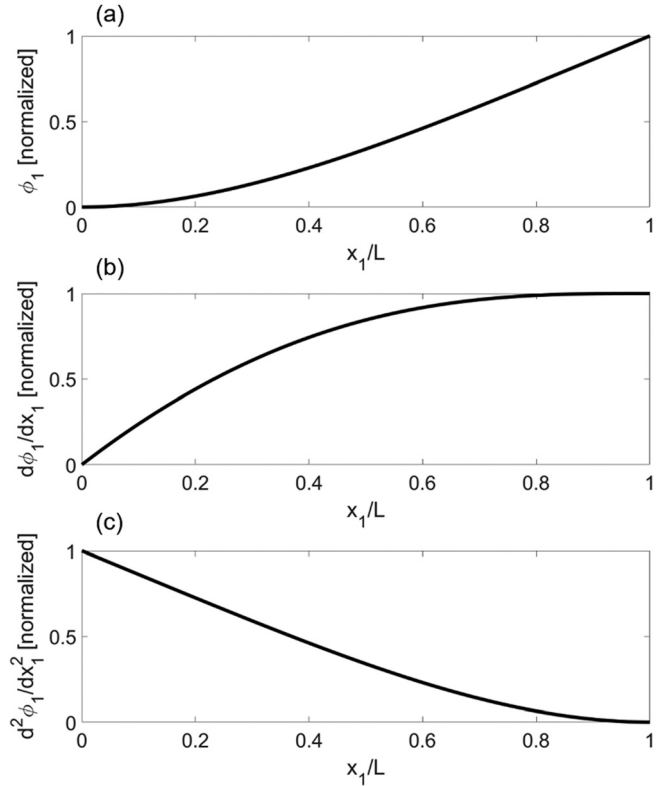


FIG. 2. Normalized (a) displacement, (b) slope, and (c) curvature distributions of a thin cantilever for the fundamental bending vibration mode ( $r = 1$ ). The maximum curvature is near the clamped end. The region  $0 \leq x_1 \leq L/2$  produces 85% of the modal electromechanical coupling from Eq. (22) and Fig. 2(b).

on the coupling coefficient. The Figure of Merit (FoM) in flexoelectric energy conversion is

$$\text{FoM} = \frac{\mu_{1133}^2}{c_{1111} \epsilon_{33}}, \quad (43)$$

or  $\mu_{1133}^2 / c_{1111} \chi_{33}$ , and as  $\text{FoM} \rightarrow \infty$ ,  $k^2 \rightarrow 1$  which is the limit of 100% mechanical-to-electrical energy conversion within the structure (note that it is not the percentage energy delivered to the electrical load, hence not an overall efficiency). Since  $\mu_{1133} = \chi_{33} f_{1133}$  and  $\text{FoM} \propto f_{1133}^2 \chi_{33} / c_{1111}$ , the alternative FoM forms are  $f_{1133}^2 \chi_{33} / c_{1111}$  or  $f_{1133}^2 \chi_{33} s_{1111}$  (where  $s_{1111}$  is the short-circuit elastic compliance). According to  $\text{FoM} \propto f_{1133}^2 \chi_{33} s_{1111}$ , for a fixed flexocoupling coefficient (e.g.,  $f \approx q / (4\pi \epsilon_0 a)$  based on Kogan's estimate<sup>30</sup>), softer materials with high dielectric permittivity should be preferred for increased FoM. For resonant energy harvesting purposes, the quality factor ( $Q$ ) of the material is also important, and  $k^2 Q$  should be used for comparing flexoelectric energy harvesting performance of different materials (and soft materials tend to be more lossy, yielding low  $Q$  values as a tradeoff). However, to explore size effects in the same single material, the coupling coefficient alone is sufficient assuming size-independent loss characteristics for simplicity (in fact, favorably, the intrinsic quality factor is expected to increase with reduced thickness according to recent molecular dynamics simulations<sup>58</sup> at the nanoscale).

## V. CASE STUDIES AND RESULTS

### A. Electromechanical coupling coefficient and size effects

The electromechanical coupling coefficient due to flexoelectric energy conversion, or simply the transverse mode flexoelectric coupling coefficient,  $k$ , is plotted for a range of FoM values and cantilever thicknesses in Fig. 3. The focus is placed on the fundamental bending vibration mode ( $r = 1$ ), and the beam thicknesses in the simulations range from 1 mm to 1 nm. Typical atomistic simulations<sup>28</sup> result in flexoelectric coefficient values on the order of  $10^{-9}$  C/m while the experimentally identified values (by Cross *et al.*<sup>36,39,59</sup> for mm-scale samples) are as high as  $10^{-4}$  C/m. As stated previously based on Eq. (42), the coupling coefficient increases with decreased thickness. This is now illustrated graphically in Fig. 3. The coupling coefficient also increases with increased flexoelectric FoM defined by Eq. (43). As a specific instance, for typical Strontium Titanate (STO) elastic<sup>60,61</sup> and dielectric<sup>24,62</sup> properties of  $c_{1111} = 318$  GPa and  $\epsilon_{33} = 2.66$  nF/m (for the room temperature relative permittivity<sup>24,42,62</sup>  $\epsilon_{33}/\epsilon_0 = 300$  – it should be mentioned that the atomistic simulations<sup>28</sup> typically assume zero temperature), and using the atomistic flexoelectric coefficient value<sup>28</sup> of  $\mu_{1133} = -3.75 \times 10^{-9}$  C/m, the resulting FoM is around  $\mu_{1133}^2/c_{1111}\epsilon_{33} = 1.66 \times 10^{-20}$  m<sup>2</sup>, yielding negligible coupling coefficient values except at the nanoscale according to Fig. 3.

Next, consider the experimental value of  $\mu_{1133} = 100 \times 10^{-6}$  C/m (the authors of the original paper<sup>36</sup> reported a positive value) for Barium Strontium Titanate (BST) from the experiments by Ma and Cross<sup>36</sup> for mm-thick samples. The elastic modulus and permittivity values of BST were reported in another work by the same group<sup>59</sup> as  $c_{1111} = 166$  GPa and  $\epsilon_{33} = 0.1594$   $\mu$ F/m, respectively. The thickness dependence of the transverse mode coupling coefficient for these properties of BST is shown in Fig. 4 (solid line), along with that of STO (dashed line) based on the aforementioned atomistic values by Maranganti and Sharma<sup>28</sup> to demonstrate the order of magnitude difference between available experiments and atomistic simulations, although the materials are not identical. As expected, with decreased thickness, the coupling

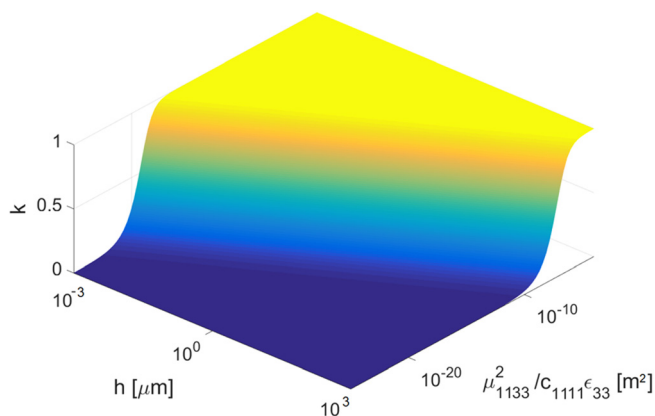


FIG. 3. Transverse mode flexoelectric coupling coefficient vs. cantilever thickness and figure of merit in flexoelectric energy conversion (for the fundamental bending vibration mode).

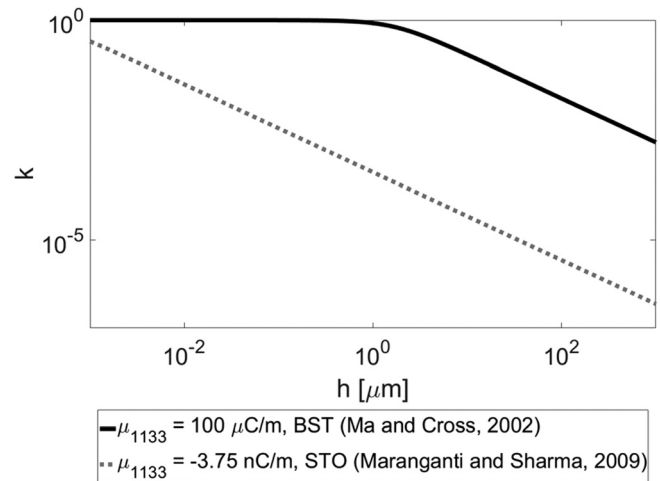


FIG. 4. Flexoelectric coupling coefficient ( $k$ ) vs. thickness ( $h$ ) plots obtained using sample flexoelectric coefficient ( $\mu_{1133}$ ) values identified by Ma and Cross<sup>36</sup> for BST (experimental) and calculated by Maranganti and Sharma<sup>28</sup> for STO (atomistic). The order of magnitude of the experimentally identified value for BST results in unrealistically high values of the coupling coefficient for all submicron thickness levels, suggesting that this coefficient identified in mm-thick samples is probably not static bulk flexoelectricity, and is not valid for small scales.

coefficient gradually approaches unity, indicating increased energy conversion with reduced thickness. Importantly, Fig. 4 reveals that, for  $\mu_{1133} = 100 \times 10^{-6}$  C/m, the coupling coefficient is nearly unity for all submicron thickness levels, which makes the validity of this value (identified from mm-thick samples<sup>36</sup>) as a bulk flexoelectric coefficient questionable. Such an order of magnitude in the bulk flexoelectric coefficient ( $\sim 10^{-4}$  C/m) suggests very high conversion even for micron-thick non-piezoelectric cantilevers, which, obviously, is not the case. This observation definitely encourages rigorous experiments at much smaller scales (ideally less than 10 nm thickness) and conditions under which the effects other than bulk flexoelectricity can be eliminated or controlled. The trend in the second curve (dashed line) based on atomistic simulations<sup>28</sup> of STO (with  $\mu_{1133} = -3.75 \times 10^{-9}$  C/m) is more reasonable, as it reveals that the coupling coefficient exceeds 0.1 only when the cantilever thickness is a few nanometers. Overall, reducing the thickness from 1 mm to 1 nm increases the flexoelectric coupling coefficient by nearly 6 orders of magnitude in the STO cantilever.

### B. Electromechanical frequency response in energy harvesting

In this section, the electromechanical frequency response of a cantilevered flexoelectric energy harvester under base excitation is simulated with a focus on the first bending mode ( $r = 1$ ) for a broad range of electrical load resistance values. Three different geometric scales are explored, spanning from mm-scale to nm-scale thickness. For each case, the length/width/thickness aspect ratio is fixed at 100/5/1. The cantilever is made of STO and has perfectly conductive surface electrodes on the faces that are perpendicular to the direction of transverse base excitation (Fig. 1). The previously mentioned atomistic value<sup>28</sup> of  $\mu_{1133} = -3.75 \times 10^{-9}$  C/m is used in the following simulations

along with the relevant material properties:<sup>60,61</sup>  $c_{1111} = 318$  GPa,  $\epsilon_{33} = 2.66$  nF/m, and  $\rho = 5116$  kg/m<sup>3</sup>. A mechanical quality factor ( $Q$ ) of  $\sim 50$  is assumed, yielding an approximate modal mechanical damping ratio of 1% of the critical damping (i.e.,  $\zeta_1 \cong 1/2Q = 0.01$  for the first bending mode). Three cases with thicknesses of 1 mm, 1  $\mu$ m, and 1 nm are analyzed to explore the effect of thickness while keeping the  $L/b/h$  aspect ratio fixed at 100/5/1. The mechanical excitation is harmonic base acceleration,  $d^2w_b(t)/dt^2 = -\omega^2 W_0 e^{j\omega t}$ . Therefore, the results are given in the form of frequency response magnitude maps normalized by the base acceleration quantified in terms of the gravitational acceleration ( $g = 9.81$  m/s<sup>2</sup>). A wide range of electrical load resistance values spanning from short- to open-circuit conditions (100  $\Omega$  to 1 G $\Omega$ ) are simulated for each case study to capture the optimal load in power generation and the respective trends with changing load.

The voltage output (per base acceleration) frequency response map (obtained from Eq. (33) via  $|v(t)/-\omega^2 W_0 e^{j\omega t}|$  as the magnitude form) for the 1 mm-thick STO beam (100 mm  $\times$  5 mm  $\times$  1 mm) is shown in Fig. 5(a). The base excitation frequency is normalized with respect to the fundamental short-circuit natural frequency in the vertical axis. With increased electrical load resistance, the voltage output increases monotonically at all frequencies, as a typical trend in energy harvesting.<sup>54</sup> It is shown that the resonance frequency for the 1 mm-thick STO cantilever is unaffected by the change in resistive load, i.e., the frequency of peak magnitude does not change as the electrical load resistance value is swept from short- to open-circuit conditions. This indicates very low electromechanical coupling such that the feedback in the mechanical domain due to induced low voltage is negligible. The flexoelectric coupling coefficient for the 1 mm thickness level and STO material property combination is obtained from Eq. (42) or Fig. 4 as  $k \approx 3.5 \times 10^{-7}$ , confirming negligible electromechanical coupling. The beam thickness is then decreased to 1  $\mu$ m while keeping the same aspect ratio (i.e., the dimensions are now 100  $\mu$ m  $\times$  5  $\mu$ m  $\times$  1  $\mu$ m) and the analysis is repeated. The voltage output frequency response map for this case is shown in Fig. 5(b). As with the 1 mm thickness case, the 1  $\mu$ m-thick STO cantilever shows no noticeable change in the fundamental resonance frequency with changing load resistance. The flexoelectric coupling coefficient of this simulation case is  $k \approx 3.5 \times 10^{-4}$ , which, again, indicates very weak electromechanical coupling. Next, the beam thickness is further decreased to 1 nm and the analysis is repeated for a 100 nm  $\times$  5 nm  $\times$  1 nm sample. As shown by the voltage output frequency response map in Fig. 5(c), this nm-thick beam exhibits a certain shift in resonance frequency from short- to open-circuit conditions, which is a manifestation of significant electromechanical coupling according to Eq. (35). Decreasing the thickness of the cantilever (while keeping the same volumetric aspect ratio) results in increased electromechanical coupling, hence increased mechanical to electrical energy conversion. The electromechanical coupling for this thickness level is  $k \approx 0.33$ , which is in agreement with nearly 5.6% difference between the values of the fundamental short- and open-circuit resonance frequencies in Fig. 5(c).

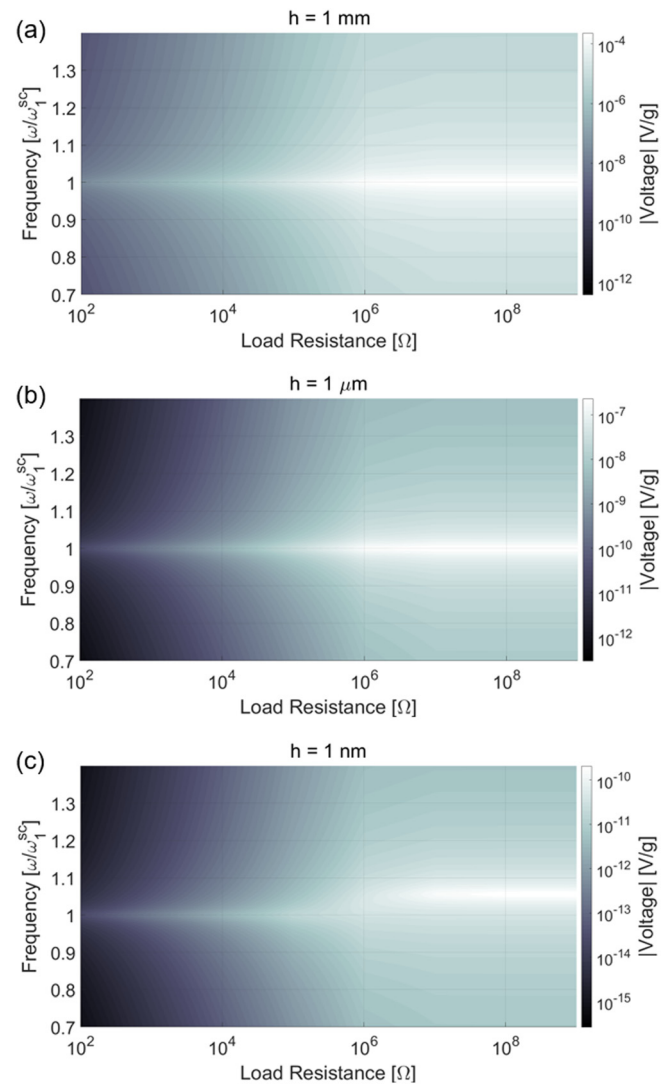


FIG. 5. Voltage output frequency response vs. load resistance maps (in magnitude form and per base acceleration) for cantilevered STO harvesters with a fixed aspect ratio of 100/5/1 ( $L/b/h$ ) for three different geometric scales with the following thickness ( $h$ ) values: (a) 1 mm, (b) 1  $\mu$ m, and (c) 1 nm.

This can easily be confirmed using Eq. (35) (for  $\omega_1^{sc}$ ,  $\omega_1^{oc}$ , and  $k$  relationship), since the *resonance* frequencies (frequencies of peak forced response magnitude) are very close to the *natural* frequencies in the lightly damped setting with  $\zeta_1 = 0.01$ .

The electric current flowing to the resistive load is simply obtained from the voltage output using Ohm's law. The current output (per base acceleration) frequency response maps (calculated using  $|v(t)/-R_l \omega^2 W_0 e^{j\omega t}|$ ) are also generated for the STO cantilever configurations of each geometric scale using the previously mentioned fixed volumetric aspect ratio as displayed in Fig. 6. The electric current decreases monotonically with increased electrical load resistance at all frequencies, which is the opposite trend as compared to the voltage output. At all frequencies, the maximum current is achieved under short-circuit conditions of the surface electrodes. As with the voltage output frequency response maps, similar trends are observed for each case study in terms of the flexoelectric coupling coefficient. The thickness levels of 1 mm and 1  $\mu$ m show no noticeable shift in resonance

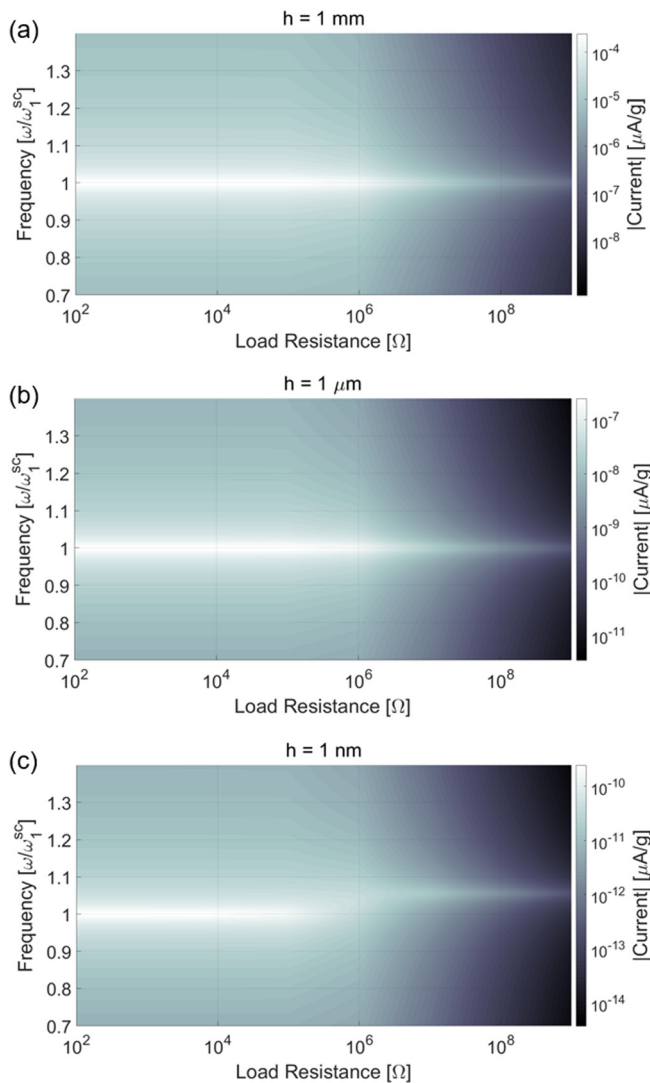


FIG. 6. Current output frequency response vs. load resistance maps (in magnitude form and per base acceleration) for cantilevered STO harvesters with a fixed aspect ratio of 100/5/1 ( $L/b/h$ ) for three different geometric scales with the following thickness ( $h$ ) values: (a) 1 mm, (b) 1  $\mu\text{m}$ , and (c) 1 nm.

frequency (Figs. 6(a) and 6(b)), indicating negligible electro-mechanical coupling, whereas the 1 nm thickness case results in significant frequency shift (Fig. 6(c)), revealing strong electromechanical coupling as discussed previously for the voltage output.

As a product of two quantities which have opposite trends with changing load resistance, the electrical power output exhibits more interesting trends, such as the presence of an optimal electrical load resulting in the maximum power output at a given frequency. The electrical power output is calculated using  $|v(t)/-\omega^2 W_0 e^{i\omega t}|^2/R_l$  (which is nothing but the product of the voltage and current figures) for each of the three geometric scales and the fixed aspect ratio discussed previously. The resulting graphs are shown in Fig. 7. Note that, since the output voltage and current are individually proportional to the base acceleration, the power output is proportional to base acceleration squared (hence normalized by  $g^2$ ), i.e., doubling the base acceleration increases the power output by a factor of 4 under the linear system assumption. The optimal load for peak power output can be

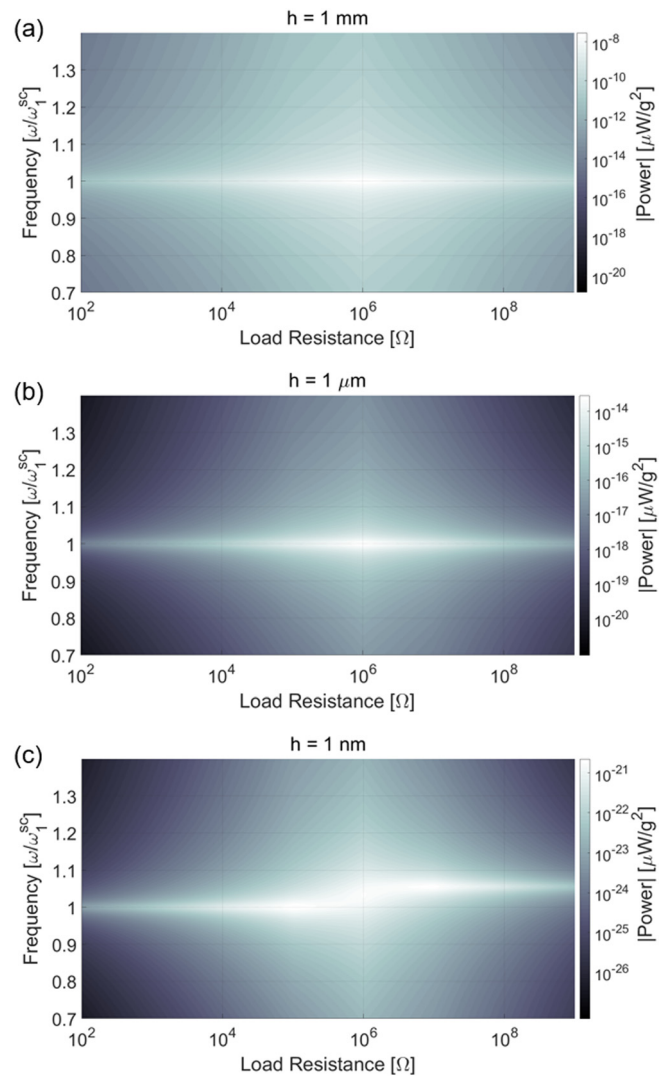


FIG. 7. Power output frequency response vs. load resistance maps (in magnitude form and per base acceleration squared) for cantilevered STO harvesters with a fixed aspect ratio of 100/5/1 ( $L/b/h$ ) for three different geometric scales with the following thickness ( $h$ ) values: (a) 1 mm, (b) 1  $\mu\text{m}$ , and (c) 1 nm.

determined for each case from the power output frequency response maps. For instance, the cases of both 1 mm and 1  $\mu\text{m}$ -thick harvesters result in a peak power output around 1 M $\Omega$  (Figs. 7(a) and 7(b)). As with the previous frequency response maps, the 1 mm and 1  $\mu\text{m}$  power output frequency response maps show the resonance frequency to be insensitive to the resistive load due to very low electromechanical coupling. Consequently, a single optimal load is observed in the power map for the fundamental vibration mode. On the other hand, the 1 nm case study exhibits two peak values for two distinct optimal electrical loads, 100 k $\Omega$  and 10 M $\Omega$ , respectively, at the short-circuit and open-circuit resonance frequencies, yielding the same power output. The existence of two peaks in the power output is also the case in strongly coupled and lightly damped piezoelectric energy harvesters.<sup>54,63,64</sup> The same power output can be extracted at the short-circuit resonance frequency ( $\sim\omega_1^{sc}$ ) for a lower electrical load resistance or at the open-circuit resonance frequency ( $\sim\omega_1^{oc}$ ) for a larger electrical load resistance. As a result, the

former optimal condition results in larger current and lower voltage, while the latter gives larger voltage and lower current, which can also be confirmed with Figs. 5 and 6. On the practical side of energy harvesting implementation, in some cases higher voltage is preferred, such as in AC-DC conversion using a rectifier, in order to overcome forward bias voltage of diodes, when charging a storage component. In other scenarios (if the voltage output is not an issue), higher current may be preferred, e.g., to charge a storage component faster. Note that, with reduced thickness from mm to nm in Fig. 7, the resonant electrical power magnitude for a fixed base acceleration intensity decreases substantially (by 13 orders of magnitude); however, the volume also decreases (by 18 orders of magnitude); hence, the power density increases by a factor of about  $10^5$  if the mechanical base acceleration magnitude is kept the same.

Finally, it is of interest to explore what happens to the structural response of the STO cantilever while generating electricity from strain gradient fluctuations in response to mechanical base excitation. The motion of the cantilever can be evaluated at any position ( $x_1$ ) using Eq. (34), while the focus is typically placed on the tip ( $x_1 = L$ ). Figure 8 shows the tip displacement map (per base acceleration input via  $|w_{rel}(L, t) / -\omega^2 W_0 e^{i\omega t}|$ ) for the cantilevers of all three geometric scales using the same load resistance and normalized excitation frequency ranges discussed previously. For the cases of 1 mm and  $1 \mu\text{m}$  thickness levels, as another manifestation of very weak electromechanical coupling at these geometric scales, the vibration response of the cantilever is insensitive to changing electrical load resistance (Figs. 8(a) and 8(b)). That is, although some power output is delivered to the electrical load according to Figs. 7(a) and 7(b), the level of this electrical output is so small that it is negligible as compared to mechanical (vibrational) energy of the harvester (confirmed by the coupling coefficient values); and this tiny level of electricity production does not alter the vibration response although the converse effect is taken into account in the model (i.e., the converse flexoelectric effect is negligible at these geometric scales). Therefore, as a result of weak electromechanical coupling, Joule heating in the resistive load does not create any significant dissipation in the vibration response of the STO cantilever. However, for the cantilever with 1 nm thickness, as we know from the previous electrical output graphs (Figs. 5(c), 6(c), and 7(c)), the electromechanical coupling is relatively strong, and therefore, mechanical to electrical energy conversion is rather significant. As a consequence, the response of the harvester is sensitive to changing electrical load in Fig. 8(c) in the vicinity of the resonance. Certain load resistance values result in significant shunt damping, analogous to piezoelectric shunt damping,<sup>65</sup> confirming thermodynamic consistency of the fully coupled electroelastodynamic model.

## VI. CONCLUSIONS

An electroelastodynamic framework is developed and analyzed for flexoelectric energy harvesting from strain gradient fluctuations in centrosymmetric dielectrics, by accounting for the presence of a finite electrical load across the

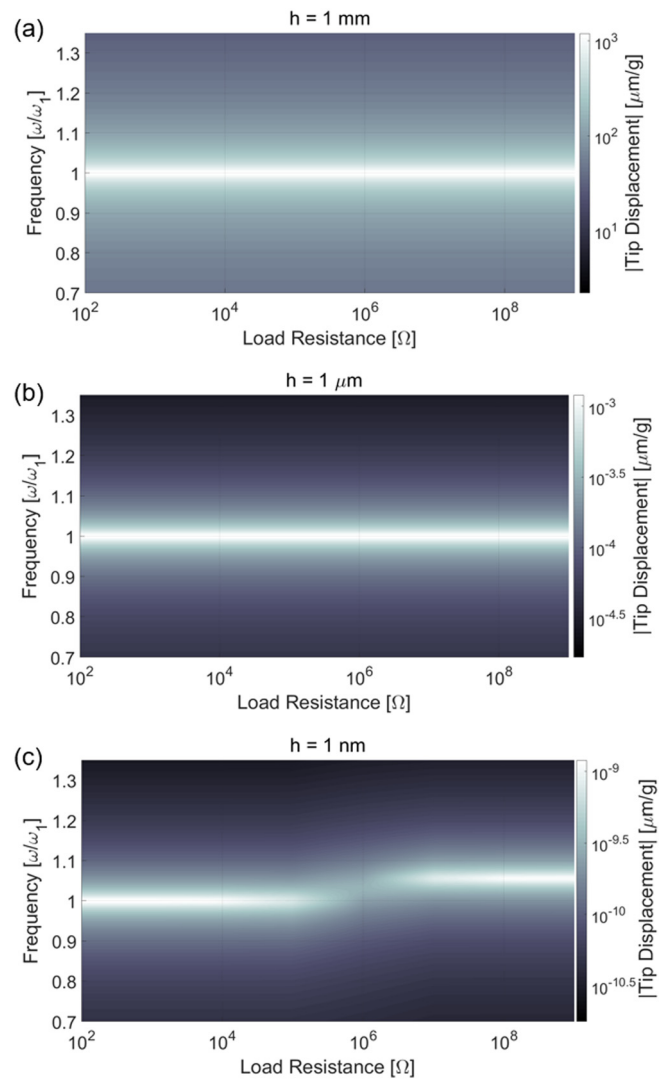


FIG. 8. Tip displacement frequency response vs. load resistance maps (in magnitude form and per base acceleration) for cantilevered STO harvesters with a fixed aspect ratio of 100/5/1 ( $L/b/h$ ) for three different geometric scales with the following thickness ( $h$ ) values: (a) 1 mm, (b)  $1 \mu\text{m}$ , and (c) 1 nm.

surface electrodes as well as two-way electromechanical coupling. The flexoelectric energy harvester model presented in this work is based on the Euler-Bernoulli beam theory and it assumes the main source of polarization to be static bulk flexoelectricity. Following recent efforts on the converse flexoelectric effect in finite samples, the proposed model properly accounts for thermodynamically consistent, symmetric, direct and converse coupling terms, and it captures the size effect on the coupling coefficient.

Based on a modal analysis procedure, closed-form solutions of the electromechanical frequency response functions (voltage across the electrical load and coupled vibration response) are given. Results of an extensive analysis are presented at different geometric scales (mm,  $\mu\text{m}$ , and nm thickness levels with a fixed aspect ratio) for a Strontium Titanate (STO) cantilever that is shunted to a resistive electrical load for quantifying the electrical power output and its feedback on the vibration response due to the converse effect. Harmonic excitation is assumed and the focus of the

numerical study is placed on the fundamental bending mode, which is the most flexible mode and it results in no charge cancellation when continuous surface electrodes are employed. However, the model can be employed for higher vibration modes, segmented electrodes, as well as other deterministic or random mechanical excitation forms.

The transverse mode flexoelectric coupling coefficient,  $k$ , (as a direct and compact measure of energy conversion) is analytically extracted from the short- and open-circuit natural frequencies. Dependence of the coupling coefficient on the thickness and material parameters (figure of merit) is discussed in detail. The flexoelectric energy conversion and harvesting become significant only at nm thickness levels for typical flexoelectric coefficients obtained from atomistic simulations (with an order of magnitude  $\sim 10^{-9}$  C/m). For instance, the negligible flexoelectric coupling of an STO cantilever at the mm thickness level increases by 6 orders of magnitude (from  $k \approx 3.5 \times 10^{-7}$  to  $k \approx 0.33$ ) when the thickness is reduced to nm-level. It is no surprise that the flexoelectric power output of an individual nanoscale centrosymmetric dielectric cantilever is very low (Fig. 8). However, the quantitative understanding of this size dependence provided by the presented framework could help the designer tailor the individual beam dimensions (cross section for bending vibrations) and fabricate a cluster of flexoelectric energy harvesters to maximize energy conversion under the constraints of a fixed material volume, target frequency range, among other parameters.

Substantially high values of flexoelectric coefficients ( $\sim 10^{-4}$  C/m) reported in the literature based on experiments conducted with mm-thick samples result in extremely high values of the coupling coefficient ( $k$ ), yielding values nearly unity for all submicron thickness levels, and therefore suggesting very high energy conversion even at the  $\mu\text{m}$  thickness level, which is not the case in reality. This observation confirms that the identified constants for certain mm-thick samples probably do not represent bulk flexoelectricity and are not valid at other scales (and cannot be used in the proposed model). Therefore, the need for rigorous experiments at smaller scales is pointed out (at submicron scales, and preferably for less than 10 nm sample thickness, by eliminating or controlling the effects other than bulk flexoelectricity). Overall, the proposed framework can be used not only for flexoelectric energy harvesting, but also for sensing, actuation, and parameter identification in experiments conducted at various geometric scales within the limits of continuum electroelastodynamics. While this work has considered static bulk flexoelectricity alone, future electroelastodynamic modeling efforts may consider incorporating surface piezoelectricity and flexoelectricity,<sup>24,25</sup> as well as size-dependence of the quality factor due to intrinsic dissipation mechanisms<sup>58</sup> (since  $k^2Q$  is a more complete figure of merit for resonant energy harvesting).

## ACKNOWLEDGMENTS

This work was supported by the National Science Foundation Grant No. CMMI-1463339, which is gratefully acknowledged.

- <sup>1</sup>K. Cook-Chennault, N. Thambi, and A. Sastry, *Smart Mater. Struct.* **17**(4), 043001 (2008).
- <sup>2</sup>J. Q. Liu, H. B. Fang, Z. Y. Xu, X. H. Mao, X. C. Shen, D. Chen, H. Liao, and B. C. Cai, *Microelectron. J.* **39**(5), 802–806 (2008).
- <sup>3</sup>W. J. Choi, Y. Jeon, J. H. Jeong, R. Sood, and S. G. Kim, *J. Electroceram.* **17**(2–4), 543–548 (2006).
- <sup>4</sup>Y. Qin, X. D. Wang, and Z. L. Wang, *Nature* **451**(7180), 809–U805 (2008).
- <sup>5</sup>U. Aridogan, I. Basdogan, and A. Erturk, *J. Intell. Mater. Syst. Struct.* **25**(14), 1664–1680 (2014).
- <sup>6</sup>M. Carrara, M. Cacan, J. Toussaint, M. Leamy, M. Ruzzene, and A. Erturk, *Smart Mater. Struct.* **22**(6), 065004 (2013).
- <sup>7</sup>S. Tol, F. Degertekin, and A. Erturk, *Appl. Phys. Lett.* **109**(6), 063902 (2016).
- <sup>8</sup>L. Moro and D. Benasciutti, *Smart Mater. Struct.* **19**(11), 115011 (2010).
- <sup>9</sup>N. Elvin and A. Erturk, *Advances in Energy Harvesting Methods* (Springer Science & Business Media, 2013).
- <sup>10</sup>K. A. Cunefare, E. Skow, A. Erturk, J. Savor, N. Verma, and M. Cacan, *Smart Mater. Struct.* **22**(2), 025036 (2013).
- <sup>11</sup>X.-B. Cui, C.-P. Huang, and J.-H. Hu, *J. Appl. Phys.* **117**(10), 104502 (2015).
- <sup>12</sup>S. Shahab, M. Gray, and A. Erturk, *J. Appl. Phys.* **117**(10), 104903 (2015).
- <sup>13</sup>A. Erturk, W. G. R. Vieira, C. De Marqui, and D. J. Inman, *Appl. Phys. Lett.* **96**(18), 184103 (2010).
- <sup>14</sup>C. De Marqui, Jr. and A. Erturk, *J. Intell. Mater. Syst. Struct.* **24**(7), 846–854 (2013).
- <sup>15</sup>J. Allen and A. Smits, *J. Fluids Struct.* **15**(3–4), 629–640 (2001).
- <sup>16</sup>A. Erturk and G. Delporte, *Smart Mater. Struct.* **20**(12), 125013 (2011).
- <sup>17</sup>ANSI/IEEE, Report No. 176–1987, 1984.
- <sup>18</sup>S. Trolier-McKinstry and P. Muralt, *J. Electroceram.* **12**(1–2), 7–17 (2004).
- <sup>19</sup>E. Fukada, *IEEE Trans. Ultrason., Ferroelectr. Freq. Control* **47**(6), 1277–1290 (2000).
- <sup>20</sup>M. D. Maeder, D. Damjanovic, and N. Setter, *J. Electroceram.* **13**(1–3), 385–392 (2004).
- <sup>21</sup>M. Majdoub, P. Sharma, and T. Cagin, *Phys. Rev. B* **77**(12), 125424 (2008).
- <sup>22</sup>A. Tagantsev, *Phys. Rev. B* **34**(8), 5883 (1986).
- <sup>23</sup>A. K. Tagantsev, V. Meunier, and P. Sharma, *MRS Bull.* **34**(09), 643–647 (2009).
- <sup>24</sup>P. Zubko, G. Catalan, and A. K. Tagantsev, *Annual Rev. Mater. Res.* **43**, 387–421 (2013).
- <sup>25</sup>P. Yudin and A. Tagantsev, *Nanotechnology* **24**(43), 432001 (2013).
- <sup>26</sup>T. D. Nguyen, S. Mao, Y. W. Yeh, P. K. Purohit, and M. C. McAlpine, *Adv. Mater.* **25**(7), 946–974 (2013).
- <sup>27</sup>J. Zhang, C. Wang, and C. Bowen, *Nanoscale* **6**(22), 13314–13327 (2014).
- <sup>28</sup>R. Maranganti and P. Sharma, *Phys. Rev. B* **80**(5), 054109 (2009).
- <sup>29</sup>V. Mashkevich and K. Tolpygo, *Sov. Phys. JETP* **5**(3), 435–439 (1957).
- <sup>30</sup>S. M. Kogan, *Sov. Phys.-Solid State* **5**(10), 2069–2070 (1964).
- <sup>31</sup>V. Indenbom, E. Loginov, and M. Osipov, *Kristallografiya* **26**(6), 1157–1162 (1981).
- <sup>32</sup>A. Buka and N. Éber, *Flexoelectricity in Liquid Crystals: Theory, Experiments and Applications* (World Scientific, 2012).
- <sup>33</sup>A. G. Petrov, *Biochim. Biophys. Acta* **1561**(1), 1–25 (2002).
- <sup>34</sup>W. Ma and L. E. Cross, *Appl. Phys. Lett.* **79**(26), 4420–4422 (2001).
- <sup>35</sup>W. H. Ma and L. E. Cross, *Appl. Phys. Lett.* **78**(19), 2920–2921 (2001).
- <sup>36</sup>W. Ma and L. E. Cross, *Appl. Phys. Lett.* **81**(18), 3440–3442 (2002).
- <sup>37</sup>W. H. Ma and L. E. Cross, *Appl. Phys. Lett.* **82**(19), 3293–3295 (2003).
- <sup>38</sup>W. H. Ma and L. E. Cross, *Appl. Phys. Lett.* **86**(7), 072905 (2005).
- <sup>39</sup>W. H. Ma and L. E. Cross, *Appl. Phys. Lett.* **88**(23), 232902 (2006).
- <sup>40</sup>L. E. Cross, *J. Mater. Sci.* **41**(1), 53–63 (2006).
- <sup>41</sup>P. Zubko, G. Catalan, A. Buckley, P. Welche, and J. Scott, *Phys. Rev. Lett.* **99**(16), 167601 (2007).
- <sup>42</sup>P. Zubko, G. Catalan, A. Buckley, P. Welche, and J. Scott, *Phys. Rev. Lett.* **100**(19), 199906 (2008).
- <sup>43</sup>W. Huang, K. Kim, S. Zhang, F. G. Yuan, and X. Jiang, *Phys. Status Solidi RRL* **5**(9), 350–352 (2011).
- <sup>44</sup>M. Majdoub, P. Sharma, and T. Çağın, *Phys. Rev. B* **78**(12), 121407 (2008).
- <sup>45</sup>Q. Deng, M. Kammoun, A. Erturk, and P. Sharma, *Int. J. Solids Struct.* **51**(18), 3218–3225 (2014).
- <sup>46</sup>P. Harris, *J. Appl. Phys.* **36**(3), 739–741 (1965).
- <sup>47</sup>E. V. Bursian and O. I. Zaikovskii, *Sov. Phys. Solid State* **10**(5), 1121–1124 (1968).

- <sup>48</sup>R. D. Mindlin, *Int. J. Solids Struct.* **4**(6), 637–642 (1968).
- <sup>49</sup>A. K. Tagantsev and A. S. Yurkov, *J. Appl. Phys.* **112**(4), 044103 (2012).
- <sup>50</sup>H. Le Quang and Q.-C. He, paper presented at the Proceedings of the Royal Society of London A: Mathematical, Physical and Engineering Sciences (2011).
- <sup>51</sup>L. Shu, X. Wei, T. Pang, X. Yao, and C. Wang, *J. Appl. Phys.* **110**(10), 104106 (2011).
- <sup>52</sup>P. Yudin, R. Ahluwalia, and A. Tagantsev, *Appl. Phys. Lett.* **104**(8), 082913 (2014).
- <sup>53</sup>A. Erturk and D. J. Inman, *ASME J. Vib. Acoust.* **130**(4), 041002 (2008).
- <sup>54</sup>A. Erturk and D. J. Inman, *Piezoelectric Energy Harvesting* (John Wiley & Sons, 2011).
- <sup>55</sup>S. Leadenham and A. Erturk, *Nonlinear Dyn.* **79**(3), 1727–1743 (2015).
- <sup>56</sup>S. Leadenham and A. Erturk, *J. Sound Vib.* **333**(23), 6209–6223 (2014).
- <sup>57</sup>G. A. Lesieutre and C. L. Davis, *Proc. SPIE* **3041**, 281–292 (1997).
- <sup>58</sup>K. Kunal and N. Aluru, *J. Appl. Phys.* **116**(9), 094304 (2014).
- <sup>59</sup>J. Y. Fu, W. Zhu, N. Li, and L. E. Cross, *J. Appl. Phys.* **100**(2), 024112 (2006).
- <sup>60</sup>R. Bell and G. Rupprecht, *Phys. Rev.* **129**(1), 90 (1963).
- <sup>61</sup>A. Kityk, W. Schranz, P. Sondergeld, D. Havlik, E. Salje, and J. Scott, *Phys. Rev. B* **61**(2), 946 (2000).
- <sup>62</sup>K. Abe and S. Komatsu, *Jpn. J. Appl. Phys., Part 1* **31**(9S), 2985 (1992).
- <sup>63</sup>Y. Shu and I. Lien, *Smart Mater. Struct.* **15**(6), 1499 (2006).
- <sup>64</sup>Y. Shu and I. Lien, *J. Micromech. Microeng.* **16**(11), 2429 (2006).
- <sup>65</sup>G. A. Lesieutre, G. K. Ottman, and H. F. Hofmann, *J. Sound Vib.* **269**(3), 991–1001 (2004).